minerals

MDPI

Article

Hyperspectral Mineral Mapping and Alteration Zonation for Mineral Prospectivity: A Multi-Source Remote Sensing Case Study from Turkey

Chenli Xue [1], Jinzhong Yang [1], Dandan Wei [1], Xiang Qin [1,*], Wenjia Xu [1], Shuai Zhang [1], Yanan Zhang [1], Huiqiong Zhang [2], Jianping Chen [3], Yiwen Pan [4], Cheng Zhang [5] and Xiaofei Yang [6]

[1] China Aero Geophysical Survey and Remote Sensing Center for Natural Resources, Beijing 100083, China
[2] Beijing Institute of Geology for Mineral Resources, Beijing 100012, China
[3] School of Earth Sciences and Resources, China University of Geosciences, Beijing 100083, China
[4] Civil-Military Integration Center of China Geological Survey, Chengdu 610036, China
[5] Tianjin Center, China Geological Survey, Tianjin 300170, China
[6] Civil Aviation Research Base (Beijing) Co., Ltd., Beijing 100621, China
* Correspondence: qinxiangcags@yeah.net

Abstract

Hydrothermal alterations in the Hod Maden and Cevizlidere districts (Tethyan Metallogenic Belt, Turkey) is developed in mid- to high-altitude terrain, where conventional mapping is costly. The present study aims to evaluate a multi-source remote sensing workflow for hyperspectral mineral mapping and alteration zonation in such terrains. Iron oxide and hydroxyl anomalies were first extracted from the Landsat-9 and ASTER imagery using the Crosta principal component analysis, providing a regional framework. Alteration minerals were then identified from ZY1-02E and GF-5B AHSI data with the Spectral Angle Mapper. Multispectral anomalies define the regional alteration footprint, whereas hyperspectral data resolve the mineral assemblages within it as follows: at Cevizlidere, muscovite, chlorite, epidote and calcite delineate the phyllic and propylitic zones within the already documented concentric porphyry system; and at Hod Maden, chlorite, epidote, muscovite and hematite define belt-like footwall alteration controlled by the main fault zone. These assemblages are consistent with diagnostic Al–OH (~2.20 μm) and Mg–OH/CO_3 (~2.33–2.35 μm) absorption features. Integrating lineaments, anomalies and mineral distributions, six prospective zones were delineated and are consistent with gossan and leached cap occurrences observed during the preliminary field reconnaissance. The workflow demonstrates that multi-source remote sensing can resolve alteration mineralogy and zonation in shallow-overburden terrains, while mixed pixels and vegetation cover remain the main limitations.

Keywords: hyperspectral image; structural interpretation; alteration information extraction; Hod Maden; Cevizlidere; alteration zonation

Check for updates

Academic Editor: Behnam Sadeghi

Received: 17 October 2026
Revised: 13 November 2026
Accepted: 13 November 2026
Published: 18 November 2026

Copyright: © 2026 by the authors. Licensee MDPI, Basel, Switzerland. This article is an open access article distributed under the terms and conditions of the Creative Commons Attribution (CC BY) license.

1. Introduction

Wall-rock alteration refers to a series of changes in material composition, texture, and structure that occur in the adjacent host rocks due to chemical reactions with hydrothermal fluids during magmatic–hydrothermal mineralization. It is a widespread and significant characteristic of hydrothermal ore deposits. As alteration zones are often spatially associated with orebodies and generally exhibit a broader distribution than the mineralization itself, they serve as an important prospecting indicator [1]. Firstly, the distribution of wall-rock alteration is generally more extensive than that of the orebody, making it easier to detect

during mineral exploration. Additionally, the intensity of alteration typically increases with proximity to the orebody. Therefore, alteration zones can not only indicate the morphology and location of surface orebodies but also suggest the presence of concealed orebodies at depth [2,3]. Secondly, specific types of wall-rock alteration are often associated with particular deposit types. Hence, identifying the alteration type can help predict the potential occurrence of corresponding mineral deposits. Furthermore, the assemblage and distribution patterns of alteration zones can reveal pathways of hydrothermal fluid migration during mineralization, thereby providing guidance for prospecting [4,5]. Consequently, utilizing remote sensing technology to map the spatial distribution of alteration mineral assemblages and alteration types on a large scale is of great significance for narrowing down exploration targets and improving prospecting efficiency [6,7].

Wall-rock alterations and alteration minerals exhibit unique spectral characteristics within specific spectral ranges, distinct from those of the surrounding rocks, due to differences in material composition and structural texture [8]. This constitutes the theoretical foundation for utilizing remote sensing technology to identify alteration anomalies and alteration minerals. Since the launch of Landsat-1 in 1972, which first enabled large-scale multispectral imaging of Earth, the application of geological remote sensing has evolved through over five decades of development [9]. Since then, medium- to high-spatial resolution multispectral satellite data, such as those from the Landsat series [10], ASTER [11], Sentinel-2 [12], and Worldview series [13], have become instrumental for geological tasks including alteration anomaly extraction [14], structural interpretation [15], and lithological classification [16]. Although the band configurations of the multispectral satellites cover diagnostic spectral absorption intervals of altered rocks and minerals in the visible–near-infrared (VNIR), shortwave–infrared (SWIR) and thermal infrared (TIR) ranges, their limited number of bands and relatively low spectral resolution constrain their capability. Consequently, they are primarily suitable for extracting major alteration types—such as iron oxides, hydroxyl-bearing, and carbonate minerals—yet remain insufficient for the detailed discrimination of specific mineral species [17]. Currently, hyperspectral satellites, with their numerous narrow and contiguous spectral channels spanning 400–2500 nm and a spectral resolution better than 5 nm, enable effective detection and discrimination of diagnostic absorption features of surface minerals, thereby making detailed remote sensing identification of alteration minerals feasible. The recently developed Chinese hyperspectral satellites, such as the GF-5 series and the ZY1-02 series, provide surface hyperspectral imagery at a spatial resolution of 30 m and a swath width of 60 km, offering a low-cost solution for mineralogical mapping, and these systems play a significant role in enabling fine-scale mineral identification. Therefore, integrating the complementary strengths of multispectral (high spatial resolution) and hyperspectral (high spectral resolution) remote sensing data enables a multi-scale analytical workflow. This strategy could support the delineation of alteration type distribution and intensity from regional to local scales, facilitate the precise identification of alteration minerals, enhances structural interpretation, and ultimately improves both the accuracy and comprehensiveness of geological analyses.

The Hod Maden and Cevizlidere projects in Turkey are both significant magmatic–hydrothermal deposits, situated within the Tethyan Metallogenic Belt and characterized by abundant copper, gold, and molybdenum resources [18,19]. Both projects are situated in the mountainous plateau region of Turkey, characterized by rugged and undulating terrain, which presents significant challenges for conducting large-scale traditional field geological surveys. Although both have now entered their respective mine planning and construction phases, conducting comprehensive remote sensing geological analysis across broader areas surrounding the discovered deposits remains valuable. Although multispectral and hyperspectral data have each been widely used for alteration mapping, previous studies

have generally applied them either in isolation or at a single scale, and few have tested whether a combined multi-source workflow can reliably resolve alteration mineralogy and zonation in mid- to high-altitude terrains with shallow overburden and extensive vegetation cover, where conventional field mapping is costly and regional geological, geophysical and geochemical data are scarce. The central problem addressed in the present study is therefore whether multi-source remote sensing alone, without regional geological, geophysical or geochemical support, can still provide reliable alteration and structural information for target delineation in such terrains. This work is crucial for assessing the supportive role of remote sensing technology in resource exploration and for synthesizing existing multi-source remote sensing geological elements to identify potential new exploration target areas. The main objectives of the present study were as follows: (1) to identify various linear geological structures in the study area based on high-resolution Sentinel-2 imagery; (2) to extract alteration anomalies such as iron oxide, Al–OH, and Mg–OH, and perform alteration intensity grading using Landsat and ASTER multispectral data; (3) to conduct refined identification of alteration minerals based on GF-5B and ZY-1 02E hyperspectral satellite imagery; and (4) to delineate potential mineralization prospect areas across a broader scope by comprehensively integrating remote sensing-derived geological elements, including geological structures, various alteration anomalies, and alteration mineral distributions. Ultimately, this research aims to verify and assess the supportiveness and reliability of the comprehensive analysis of various remote sensing geological information for mineral exploration under conditions that rely solely on remote sensing technology, and to provide reference and guidance for future remote sensing-based geological prospecting.

2. Geological Setting of the Case Study Areas

In the present study, the Hod Maden and Cevizlidere project areas in Turkey were selected as research targets. Both areas have been confirmed via drilling to host rich ore bodies. Therefore, conducting multi-source remote-sensing geological analysis covering these areas is of significant value for identifying other potential prospecting targets.

Turkey lies in the Alpine Orogenic Belt between the Eurasian Plate to the north, and Arabian and African Plates to the South. Four main east–west trending tectonic belts extend across the country from north to south. The tectonic belts are the Pontides, Anatolides, Taurides and Border Folds, all of which are products of continuing continental collision, subduction and sedimentation during the Mesozoic era. The Hod Maden Project is in the northern-most, Pontide Belt, within the Eastern Pontides (Tethyan) metallogenic belt, primarily hosted in Late Cretaceous volcanic–sedimentary rock sequences. The area features several key stratigraphic units, with the Turonian Çatak Formation andesitic breccia and the Santonian Kızılkaya Formation dacitic–rhyodacitic volcanic domes and breccias serving as the principal hosts for mineralization. Regional structural patterns are dominated by steeply north–northeast dipping strata, and fault systems, notably the Hod Main Fault Zone, exert significant control over the distribution of alteration and mineralization zones. The ore-forming volcanic activity was characterized by intermediate to acidic magmatism, often displaying submarine rapid-cooling textures such as spherulitic structures and columnar joints. These features indicate a co-genetic relationship between volcanogenic massive sulfide (VMS) and epithermal mineralization in the area, collectively forming the geological foundation for this high-grade gold–copper deposit [20]. The geological map of the Hod Maden area and the distribution of its structural elements are illustrated in Figure 1. The dual VMS–epithermal affinity of the Hod Maden system governs the selection of diagnostic remotely sensed criteria. The dacitic–rhyodacitic domes and andesitic breccias constitute the principal hosts, while mineralization is structurally controlled by the Hod Main Fault Zone and its NE- to NEE-trending splays; these lithologies, fault orientations and their inter-

sections with inferred volcanic centres therefore define the primary targets. Mineralogically, the footwall chlorite–sericite–epidote–calcite assemblage and supergene goethite/"limonite" after pyrite are the key indicators, with pyrite itself traced indirectly through ferric-iron staining owing to its lack of diagnostic VNIR–SWIR absorption.

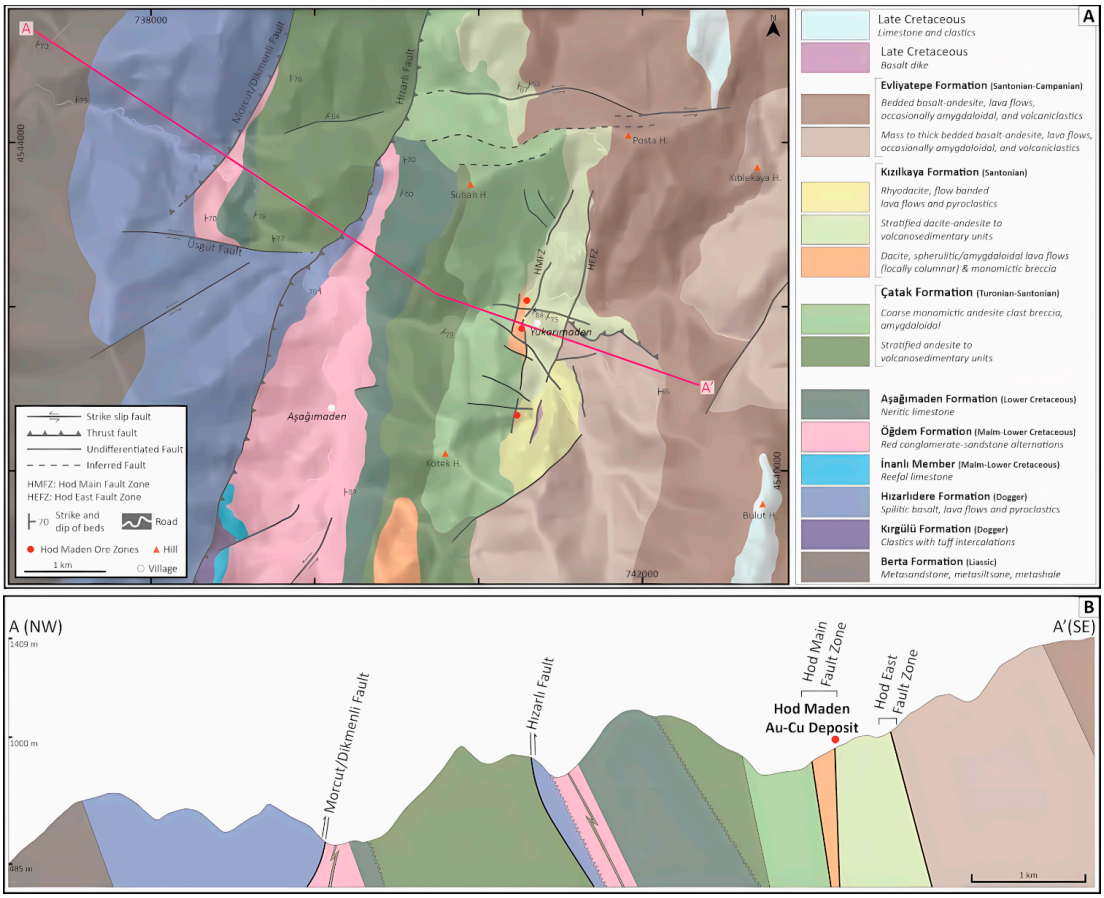


Figure 1. (**A**) Geological map of the Hod region and (**B**) the schematic A-A′ cross section showing the stratigraphic and structural association of the main rock units in the Hod Maden Au–Cu deposit (after [19]).

The Cevizlidere deposit, situated in the Tunceli Province of eastern Anatolia and is centered on a late Oligocene composite porphyritic stock intruding Paleozoic limestones and Paleogene andesitic rocks along the margin of the Ovacık pull-apart basin [21]. The mineralization is associated with medium-K, calc–alkaline diorite and granodiorite porphyries. High-precision geochronology reveals that magmatic cooling occurred at approximately 25.3 Ma, followed rapidly by hydrothermal alteration and ore formation at about 24.8 Ma [22]. This timing coincides with a major kinematic reorganization in the region, marking the transition from final subduction of the Southern Neo-Tethys oceanic slab to the incipient stages of continental collision. The intrusive rocks exhibit geochemical signatures typical of magmas derived from a subduction-modified mantle wedge. The deposit displays classic concentric alteration zoning, comprising a potassic core, an intermediate phyllic zone, and an outer propylitic halo. Its late Oligocene age distinguishes it from the region's older Eocene porphyry-epithermal systems and aligns it temporally with several early collisional porphyry deposits in central Iran, reflecting the diachronous nature of the Arabia–Eurasia collision along the Tethyan orogenic belt [23]. The geological map of the region was presented in Figure 2. The concentric potassic–phyllic–propylitic zonation of the Cevizlidere porphyry system directly constrains the extraction targets. The

phyllic zone is dominated by sericite and illite (Al-OH, ~2.20 μm), the propylitic halo by chlorite, epidote and calcite (Mg-OH/CO_3, ~2.33–2.35 μm), and the potassic core by biotite–K-feldspar–magnetite, which lacks a diagnostic hydroxyl absorption and can only be inferred indirectly; supergene goethite after pyrite in the phyllic zone accounts for the ferric-iron signature in the VNIR.

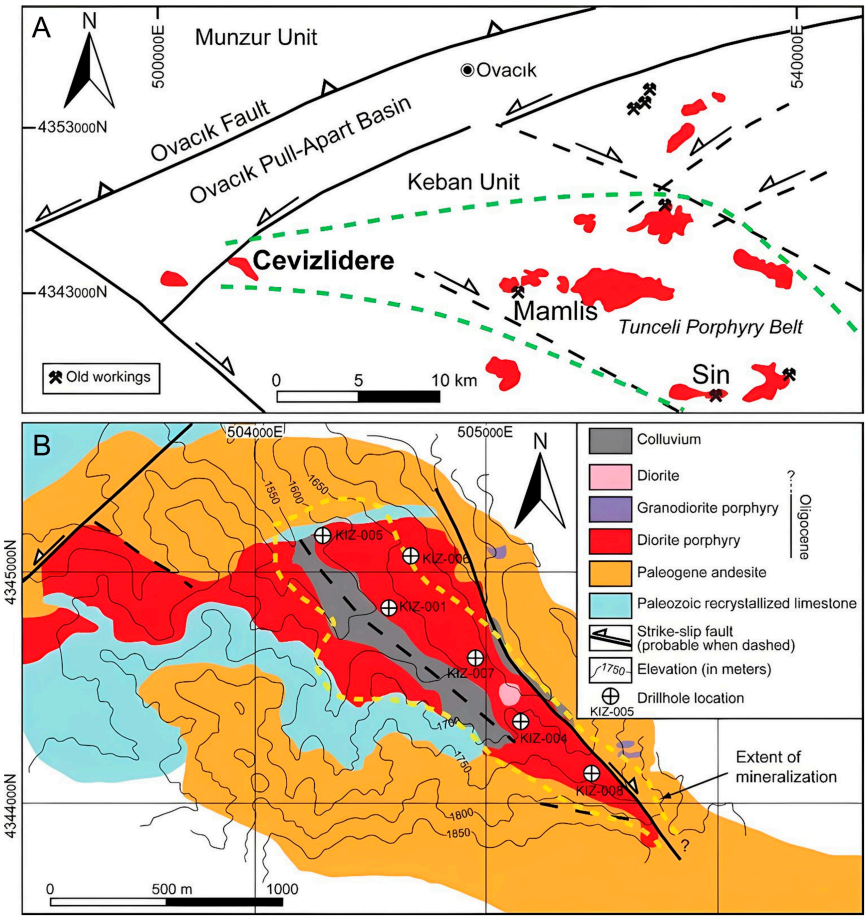


Figure 2. (**A**) Geological map showing the distribution of Oligocene intrusive centers in the Ovacık area, including the Cevizlidere prospects; (**B**) Geology of the Cevizlidere deposit (after [18]).

3. Materials and Methods

3.1. Satellite Images and Processing

3.1.1. Hyperspectral Dataset

China 5. B (GF-5B) and Ziyuan1-02D (ZY1-02E) satellites on 7 September and 26 December, 2021, respectively. Both satellites are equipped with an Advanced HyperSpectral Imager (AHSI), achieving spectral resolutions better than 5 nm in the visible to near-infrared range (VNIR) and better than 10 nm in the shortwave infrared range (SWIR), which provides critical support for fine-scale classification and feature extraction, such as surface mineral identification. Based on data availability and the requirement for cloud-free coverage over the study area, three hyperspectral satellite images—two from ZY1-02E and one from GF5B—acquired between July and October 2024, were selected for the present study. The main characteristics of the remote sensing data used in the present study were summarized in Table 1.

Table 1. Key parameters of the multispectral and hyperspectral satellites images.

Sensors	Spectral Type	Bands	Spectral Range (um)	Spatial Resolution (m)
Landsat-9 OLI2/TIRS2	VNIR	1	0.430–0.450	30
		2	0.450–0.510	30
		3	0.530–0.590	30
		4	0.640–0.670	30
		5	0.850–0.880	30
	SWIR	6	1.570–1.650	30
		7	2.110–2.290	30
	TIRS	8	10.60–11.19	100
		9	11.50–12.51	100
Sentinel-2 MSI	VNIR	1	0.458–0.523	10
		2	0.543–0.578	10
		3	0.650–0.680	10
		4	0.698–0.713	20
		5	0.733–0.748	20
		6	0.773–0.793	20
		7	0.785–0.900	10
		8	0.855–0.875	20
	SWIR	9	1.565–1.655	20
		10	2.100–2.280	20
ASTER	VNIR	1	0.520–0.600	15
		2	0.630–0.690	15
		3	0.780–0.860	15
	SWIR	4	1.600–1.700	30
		5	2.145–2.185	30
		6	2.185–2.225	30
		7	2.235–2.285	30
		8	2.295–2.365	30
		9	2.360–2.430	30
	TIR	10	8.125–8.475	90
		11	8.475–8.825	90
		12	9.925–9.275	90
		13	10.25–10.95	90
		14	10.95–11.65	90
GF-5B AHSI	VNIR	1–150	0.380–1.025	30
	SWIR	151–330	1.010–2.500	30
ZY1-02E AHSI	VNIR	1–76	0.400–1.040	30
	SWIR	77–166	1.005–2.500	30

The AHSI sensor exhibits relative low signal-to-noise ratios in the spectral bands near 400 nm and 2450 nm, and these bands have been excluded after inspection. Additionally, due to partial spectral overlap between the VNIR and SWIR regions in the hyperspectral data, only the high signal-to-noise ratio bands within the VNIR range were retained. Radiometric calibration was then performed on the hyperspectral data to convert the original digital number (DN) values recorded by the sensor into physically meaningful radiance values. Subsequently, atmospheric correction was conducted to eliminate the effects of the atmosphere on radiation transmission and to obtain an image that reflects the true surface reflectance of ground objects. However, due to the non-uniform response of the detector and on-orbit environmental interference, the hyperspectral images acquired by the push-broom imaging system of AHSI exhibit striping artifacts, particularly in the SWIR spectral range [24]. This can significantly interfere with applications such as fine mineral classification. In the present study, a moment matching method proposed by Gadallah [25] was employed to correct the striping artifacts. This global destriping approach normalizes the response of each detector column by adjusting its statistical moments (mean and

standard deviation) to match the global average across the image, and the comparisons of the bands before and after processing were presented in Figure 3. Finally, geometric registration was performed between the hyperspectral image and the Landsat 8 imagery of the same area. After the above processing steps, the hyperspectral image is used for subsequent mineral identification tasks.

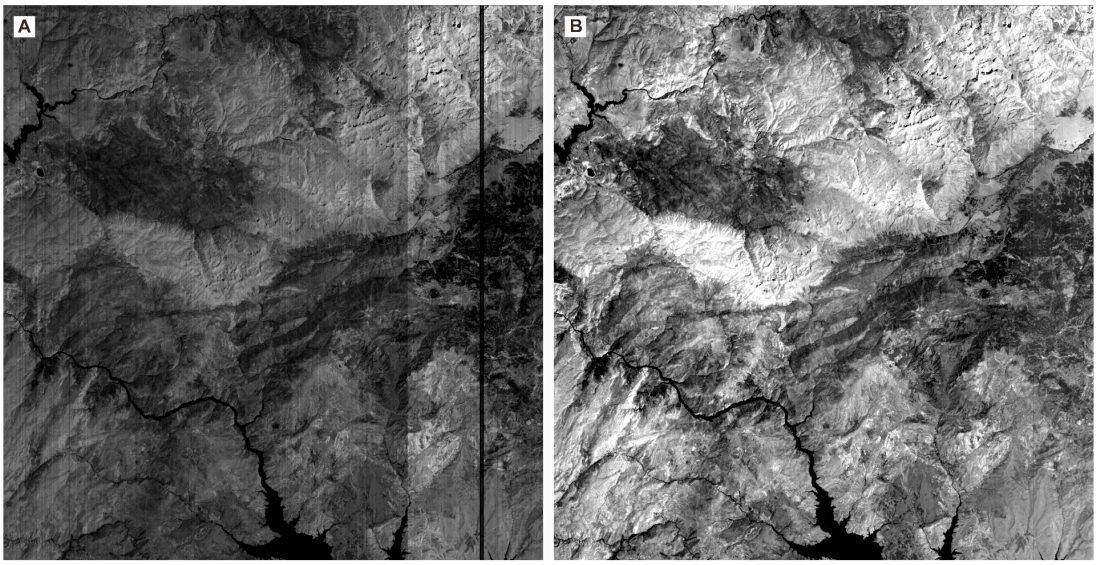


Figure 3. Comparison of hyperspectral images before and after destriping ((**A**): Before destriping; (**B**): After destriping. Taking the spectral band at the wavelength of 2048.1257 nm as an example).

3.1.2. Multispectral Dataset

For the present study, and based on the acquisition time of the hyperspectral images, Landsat-9, Sentinel-2, and Aster atmospherically corrected bi-directional surface reflectance images from the corresponding year were utilized. To mitigate interference from clouds and vegetation, all available winter images were utilized, processed for cloud removal, and subsequently used to generate a median composite image. This composite served as the foundational data for subsequent alteration information analysis and structural interpretation. All the multispectral band information of the images used was presented in Table 1.

3.2. Structural Interpretation Based on Multispectral Remote Sensing

Linear structures (primarily faults and fractures) serve as the "highways" for the migration of ore-forming materials and "favorable repositories" for their precipitation and enrichment. They exert control over every stage of the mineralization process, from fluid migration and mineral precipitation to orebody localization. The interpretation of structural faults based on multi-source remote sensing data primarily relies on detecting characteristic differences in spectral signature, tone, texture, and morphology on remote sensing imagery. These differences arise from anomalies in surface material composition, structure, geomorphology, hydrology, and vegetation induced by fault zones. In the present study, we summarized the key interpretation indicators for linear structures as follows: (1) Linear lithological boundaries, including linearly offset bedrock contacts, boundaries between bedrock and Quaternary sediments, or erosional landforms; (2) Characteristic geomorphic units shaped by fault activity, such as fault scarps, triangular facets, linear valleys, and bead-like (en echelon) lakes/depressions; (3) Offset of geomorphic units, such as displaced ridgelines and synchronous bending or displacement of drainage patterns; (4) Linear tonal differences on remote sensing imagery, evident in vegetation cover, rock masses, and shadow patterns.

Based on Sentinel-2A data combined with Google imagery, we conducted interpretations of linear structures in the study area. Firstly, spectral enhancement and false-color composition were applied to highlight alteration zones or lithological differences associated with fractures. Subsequently, based on the enhanced imagery and guided by regional geological knowledge, linear structures were identified and delineated by incorporating features such as shadows and textures from high-resolution Google imagery.

3.3. Remote Sensing Alteration Information Extraction

3.3.1. PCA-Based Analysis of Multispectral Alteration Anomalies

Principal Component Analysis (PCA) is an efficient unsupervised data dimensionality reduction method. Its essence lies in performing orthogonal transformations to convert the original correlated variables into linearly independent principal components [26], thereby achieving data dimensionality reduction and reconstruction while maximally preserving the overall variance information of the data [27]. The Crosta technique [28] is a method widely applied in remote sensing geological analysis based on PCA. It converts original image bands into uncorrelated composite variables through PCA and calculates the contribution values of the original bands to target information. By analyzing the signs and magnitudes of band loadings in the eigenvectors, it characterizes the reflectance and absorption features of surface materials and has been commonly utilized particularly in the extraction of mineral alteration information such as iron oxides and hydroxyl-bearing minerals.

As early as the 1970s, research established that different alteration minerals, due to their specific chemical structures, interact with electromagnetic waves by absorbing photons at specific wavelength ranges through electron transitions and group vibrations, thereby forming diagnostic spectral absorption features within particular electromagnetic wave ranges [29]. This establishes the physical basis for the remote sensing identification of various types of alteration lithologies. Specifically, diagnostic absorption features of iron-bearing minerals are located within the visible–near-infrared range at wavelengths of 400–900 nm, whereas hydroxyl- and carbonate-bearing alteration minerals exhibit their diagnostic absorptions in the 1900–2500 nm spectral region. For instance, minerals containing ferric ions exhibit absorption features at approximately 0.5 μm and 0.9 μm, hydroxyl group alteration minerals display diagnostic spectral absorption near 1.4 μm, 1.9 μm, and 2.2 μm, while carbonate group minerals show absorption characteristics around 0.9 μm, 1.9 μm, and 2.3 μm. According to the USGS spectral library [30,31], the spectral reflectance curves of typical alteration types are illustrated in Figure 4.

Based on the spectral absorption characteristics of different alteration minerals and the band parameters of multispectral satellites, the present study selected Landsat-9 with more bands (5) in the VNIR range for ferric-ion alteration identification, while ASTER data with more bands (6) in the SWIR range were used for analyzing hydroxyl- and carbonate-bearing alteration minerals (Table 1). By analyzing the spectral absorption positions of each alteration mineral with the corresponding multispectral satellite band ranges, the study adopted the PCA-based identification band combinations as presented in Table 2.

Table 2. Characteristics, diagnostic absorption features, and PCA-based multispectral identification model for typical alteration types.

Cation/Functional Group	Spectral Feature Range/nm	Primary Minerals		PCA-Based Spectral Combination
Fe^{2+}/Fe^{3+}	600–1100	Pyrite, Hematite, "Limonite"	Primary absorption at about 550 nm, secondary absorption at about 850 nm	Landsat-9 (B2, B4, B5, B6)

Table 2. *Cont.*

Cation/Functional Group	Spectral Feature Range/nm	Primary Minerals		PCA-Based Spectral Combination
OH	2100–2400	-	-	Landsat-9 (B2, B5, B6, B7)
Al-OH	2160–2210	Clay minerals such as illite, kaolinite, and montmorillonite	Primary absorption at about 2200 nm	Aster (B1, B3, B4, B6)
Mg-OH	2300–2400	Clay minerals such as chlorite and epidote	Primary absorption at about 2300 nm	Aster (B1, B3, B4, B8)
CO_3^{2-}	2330–2550	Calcite, Dolomite	Primary absorption at about 2350 nm, secondary absorption at about 2150 nm	Aster (B1, B5, B6, B8)
SiO_4^{4-}	8000–14,000	Quartz, Orthoclase	Primary absorption at about 10,000 nm	Aster (B10, B11, B12)

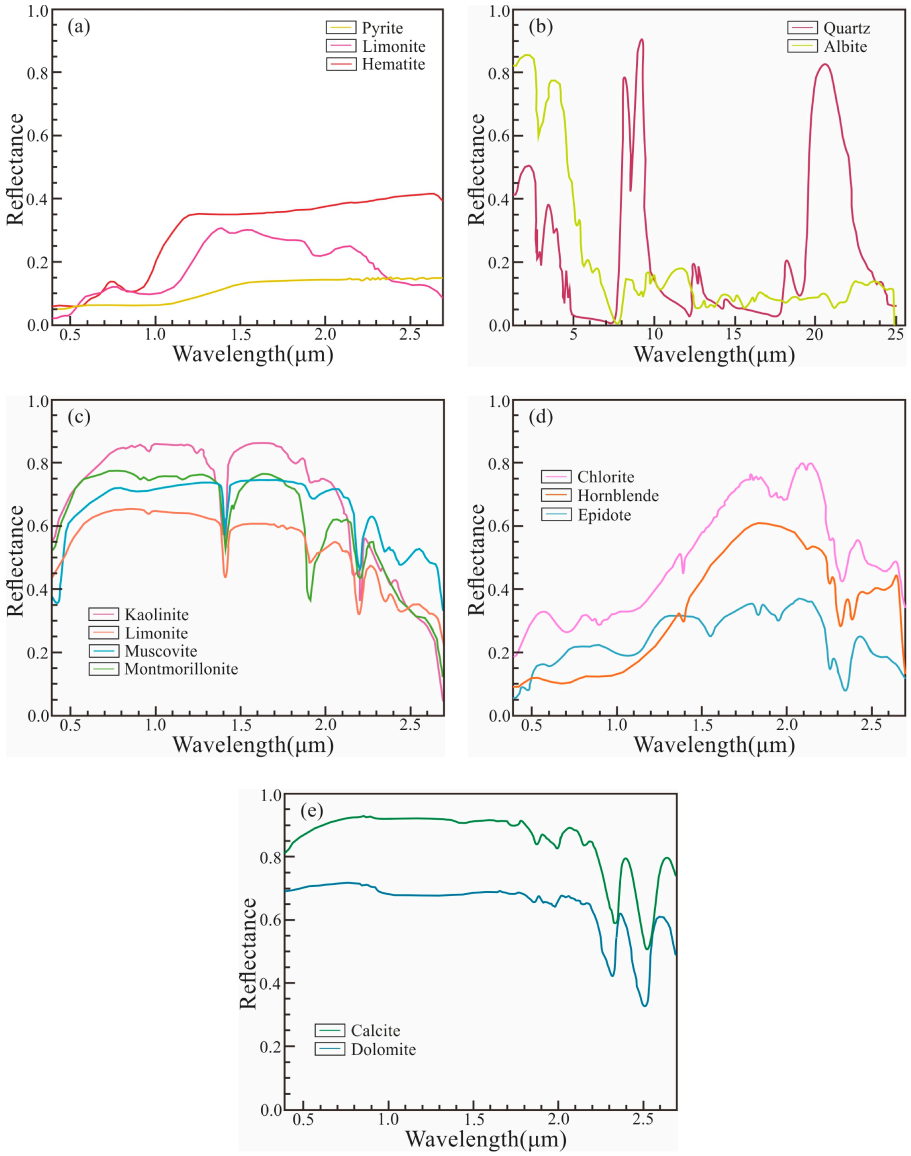


Figure 4. Spectral curve characteristics of typical alteration types ((**a**): Iron-stained alteration minerals; (**b**): Silicified alteration minerals; (**c**): Al-OH alteration minerals; (**d**): Mg-OH alteration minerals; (**e**): Carbonate alteration minerals) (after [30]).

3.3.2. Hyperspectral Image-Based Alteration Mineral Identification

Hyperspectral satellite imagery (HSI), by recording narrow and continuous spectral features of ground objects, enables the identification of diagnostic absorption characteristics of different alteration minerals and thereby offers the potential for large-scale fine-scale mineral identification. The essence of mineral identification based on HSI lies in comparing the standard spectral curves of typical minerals with the pixel spectra recorded by hyperspectral imagery and quantifying their similarity. A high degree of similarity indicates that the pixel is identified as the corresponding mineral. Spectral Angle Mapper (SAM) [32] is a well-established method for quantifying spectral similarity and has been widely applied to the identification of various alteration minerals based on HSI. In essence, this method treats the spectral curves of minerals as vectors in high-dimensional space, measuring the similarity between the two by calculating the vector angle between the standard spectral curve of a typical mineral and the spectral curve of the pixel under examination. Mathematically, SAM is the cosine of the angle between two spectral vectors, i.e., a normalized dot product, and its calculation can be formulated as follows [33]:

$$SAM(X, Y) = COS^{-1} \frac{\sum_{i=1}^{n} X_i Y_i}{\sqrt{\sum_{i=1}^{n} X_i^2} \sqrt{\sum_{i=1}^{n} Y_i^2}} \quad (1)$$

where X and Y represent the two spectral vectors, and n denotes the dimensionality of the vectors. Specifically, SAM for alteration minerals is performed based on the geological context of the study area and the USGS standard mineral spectral library. First, since the spectral range and resolution of the USGS library differ from those recorded by the HSI, the USGS mineral spectra were spectrally resampled to match the HSI spectral curves. Subsequently, the similarity between the spectral vectors of different minerals and the HSI data was quantified to achieve mineral identification.

4. Results

4.1. Structural Interpretation Distribution

The spatial distribution characteristics of linear structures in the Hod Maden and Cevizlidere areas of the Anatolian Mountains in Turkey were analyzed. Through remote sensing image enhancement and tectonic information extraction, 23 linear structures were identified in the Hod Maden area, and 32 linear structures were identified in the Cevizlidere area. The strikes of the linear structures in the Hod Maden and Cevizlidere areas are relatively consistent, both trending in two directions: NE–SW and nearly E–W. Among them, the NE–SW-trending faults exhibit relatively good extensibility and constitute the main linear structures in the region, which shows good consistency with the nearly NNE-trending deep-seated major fault, the Hod Maden Fault Zone (HMFZ), in the region. This is also in good agreement with the regional setting of these two mining areas, namely a NE-trending suture zone with Late Cretaceous island-arc volcanic rocks as the main sedimentary sequence. These faults, which are consistent with the strike of regional tectonic lines, are likely favorable channels for hydrothermal migration and, at the same time, favorable sites for mineral precipitation. Combined with the distribution of the interpreted major faults and the regional tectonic setting, it is preliminarily considered that the linear structures in this region are strongly related to deep hydrothermal migration activities, implying that this region has considerable metallogenic potential.

4.2. Alteration Anomaly Extraction Based on Multispectral Images

As shown in Table 2, the extraction of common alteration information using Landsat and ASTER multispectral data has been widely practiced based on the spectral absorption

and reflection positions of different alteration types and the band configurations of open-source satellites. Alteration phenomena such as clayization and gossan are developed in the study area. To comprehensively extract alteration information, multiple types of data were integrated for analysis. The diagnostic spectral characteristics of iron staining are primarily concentrated in the VNIR bands, while hydroxyl minerals exhibit distinct features in the SWIR bands. Consequently, long-term median imagery processed for cloud and vegetation removal within the Google Earth Engine (GEE) platform was employed, and alteration information extraction was then conducted based on the band combinations specified in Table 2.

Based on Table 2, the corresponding band combinations were used for PCA to extract alteration information. Iron-stained alteration minerals exhibit strong reflectance in Landsat-9 B4 and absorption features in B5. Therefore, in the eigenvector matrix of PCA, the coefficient corresponding to B4 should be positive, while that of B5 should be negative. The criterion for selecting the principal component of hydroxyl alteration is that the coefficients of B6 and B7 should have opposite signs, while the coefficient of B6 should have the same sign as that of B2. Therefore, principal components (bolded in Table 3) that meet the above criteria and exhibit larger absolute coefficients were selected for extracting the corresponding alteration information.

Table 3. PCA statistical result for ferric staining and hydroxyl alteration. Cevizlidere (A,C,E), Hod Maden (B,D,F).

Alteration Types	(A) Eigenvectors	OLI2	OLI4	OLI5	OLI6
Fe^{2+}/Fe^{3+}	PC1	0.229363	0.454422	0.435015	0.742735
	PC2	**0.267435**	**0.419372**	**−0.852609**	**0.160200**
	PC3	−0.362724	−0.602794	−0.288211	0.649619
	PC4	0.862729	−0.504249	0.027471	0.026003
	(B) Eigenvectors	**OLI2**	**OLI4**	**OLI5**	**OLI6**
	PC1	0.223047	0.384905	0.627341	0.639172
	PC2	**0.281030**	**0.486326**	**−0.751310**	**0.346472**
	PC3	−0.503722	−0.500517	−0.201255	0.674717
	PC4	0.785835	−0.604001	−0.038383	0.127171
Al-OH	**(C) Eigenvectors**	**ASTER1**	**ASTER3**	**ASTER4**	**ASTER6**
	PC1	0.256476	0.489767	0.68112	0.480025
	PC2	0.358854	0.739562	−0.350769	−0.44859
	PC3	0.745891	−0.277104	−0.401325	0.45365
	PC4	**−0.49909**	**0.36931**	**−0.501971**	**0.602117**
	(D) Eigenvectors	**ASTER1**	**ASTER3**	**ASTER4**	**ASTER6**
	PC1	−0.271013	−0.54086	−0.657715	−0.448814
	PC2	−0.435226	−0.66673	0.535629	0.281339
	PC3	0.821804	−0.505593	−0.091022	0.246432
	PC4	**−0.248532**	**0.085542**	**−0.521755**	**0.811595**
Mg-OH	**(E) Eigenvectors**	**ASTER1**	**ASTER3**	**ASTER4**	**ASTER8**
	PC1	0.275065	0.525763	0.725291	0.349092
	PC2	0.357508	0.718265	−0.568101	−0.18315
	PC3	0.859232	−0.452845	−0.101269	0.215399
	PC4	**−0.241346**	**0.050987**	**−0.375444**	**0.893417**
	(F) Eigenvectors	**ASTER1**	**ASTER3**	**ASTER4**	**ASTER8**
	PC1	−0.285923	−0.570684	−0.691736	−0.337741
	PC2	−0.418549	−0.648255	0.573633	0.274825
	PC3	0.822937	−0.482457	−0.082905	0.288334
	PC4	**−0.256592**	**0.146015**	**−0.430783**	**0.852799**

Based on the selected principal components, the "mean + n*standard deviations" method was employed to analyze the intensity of alteration anomalies. In this method, the mean (μ) and standard deviation (σ) of the pixel values of each selected component are calculated, and pixels with values greater than $\mu + n \times \sigma$ are classified as anomalies, while the rest are treated as background; because the threshold is defined relative to the local statistical distribution rather than an arbitrary fixed value, it adapts to the background and reduces subjective bias. Generally, for the iron-stained alteration, thresholds of n = 1.5, 2, and 2.5 were used to define low, medium, and high anomaly zones, respectively. For hydroxyl alteration, corresponding thresholds of n = 2, 2.5, and 3 were applied. Subsequently, the preliminary results were further processed with median filtering to suppress noise, and potential false anomalies such as mountain shadows were eliminated through manual visual inspection. The extracted alteration information for the two regions was presented in Figures 5 and 6.

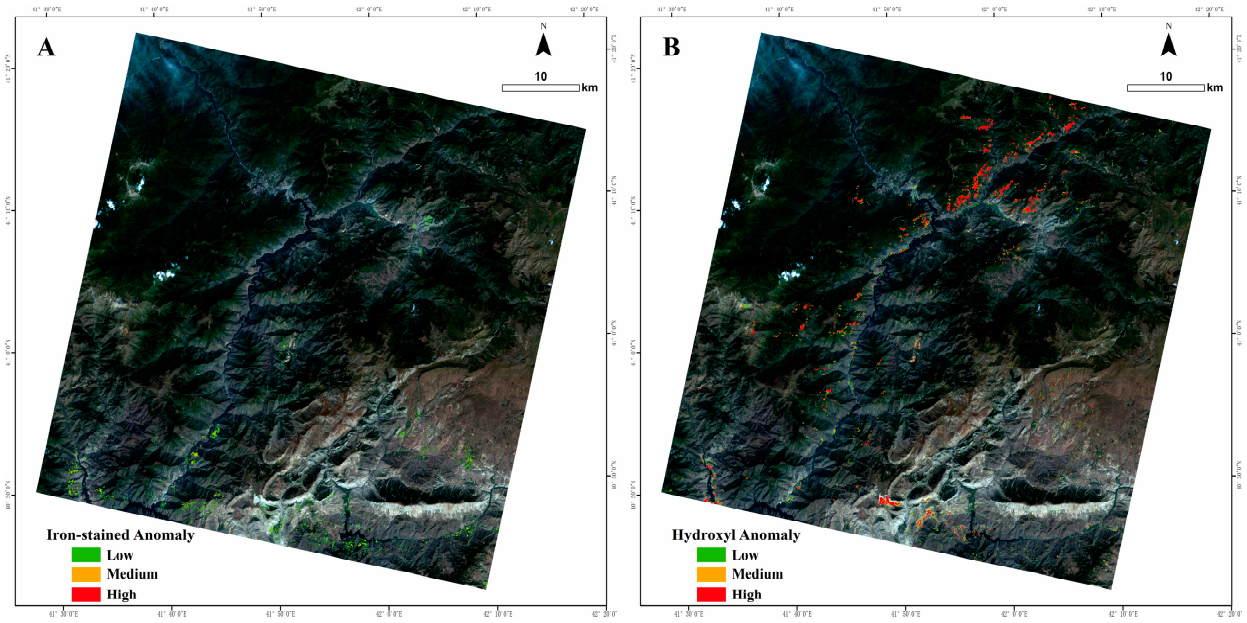


Figure 5. Extraction results of iron staining and hydroxyl alteration in the Hod Maden region based on multispectral imagery ((**A**): Iron staining; (**B**): Hydroxyl alteration. Basemap for display only; not original data).

4.3. Alteration Mineral Distribution Based on Hyperspectral Imagery

Based on the acquired two scenes of ZY1-02D and one scene of GF-5B hyperspectral imagery covering the Hod Maden and Cevizlidere areas, fine identification of alteration minerals was conducted. Preliminary field reconnaissance revealed the development of propylitization, argillic alteration, potassic alteration, and limonitization within the mining area. Therefore, the corresponding alteration mineral spectra from the USGS standard mineral spectral library were first spectrally resampled to match the spectral range and resolution of the hyperspectral satellites. Subsequently, the Spectral Angle Mapper (SAM) was applied pixel-by-pixel to compare the image spectra with the standard mineral spectra for similarity assessment. Finally, mineral identification was accomplished through dynamic threshold adjustment combined with regional geological context.

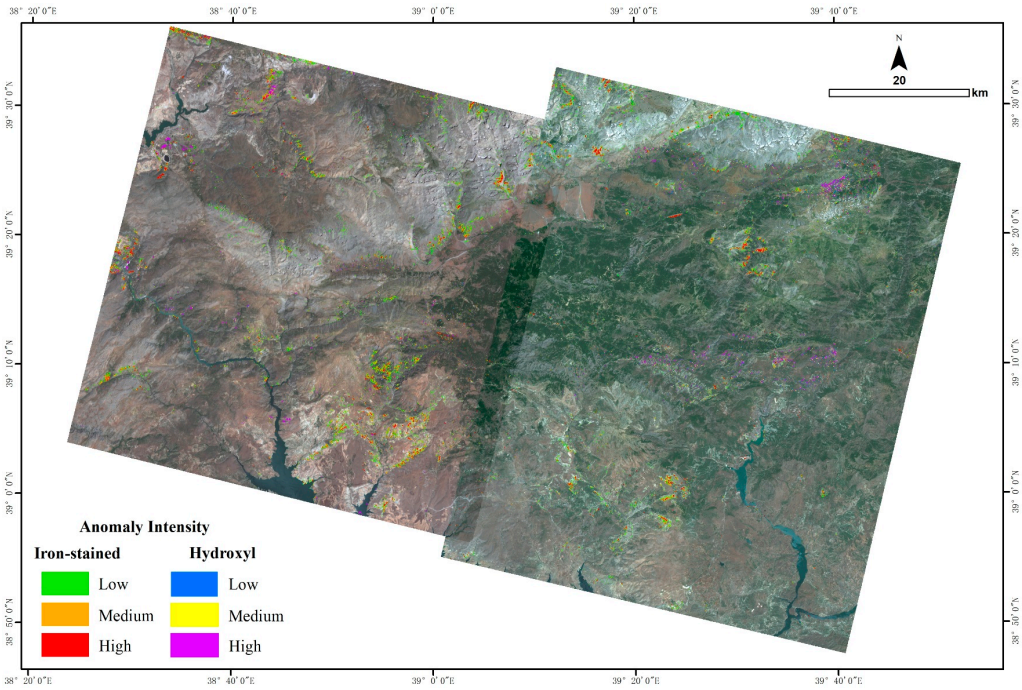


Figure 6. Extraction results of iron staining and hydroxyl alteration in the Cevizlidere region based on multispectral imagery.

The alteration mineral identification results for the Hod Maden and Cevizlidere areas were shown in Figure 7 and Figure 8, respectively. In the Hod Maden area, despite extensive vegetation cover and only sporadic bedrock exposures, the SAM demonstrated high reliability, effectively identifying mineral distributions in the southern and limited northern outcrop areas (Figure 7). As shown in Figure 8, although the two scenes of ZY1-02D and the GF-5B hyperspectral imagery covering the area differ in band count and spectral resolution, the extracted alteration minerals—such as chlorite, epidote, hematite, and muscovite—in the northern plateau mountainous region exhibit spatially consistent distribution patterns, further validating the effectiveness of the method. Vegetated areas were successfully excluded, and alteration minerals were effectively identified even on mountaintops with minimal rock exposure.

4.4. Delineation of Potential Mineral Prospects

By acquiring information such as linear structures, lithological alterations, and alteration mineral distributions in the target area through high-resolution multi-source remote sensing data, and combining this with the regional tectonic setting, favorable metallogenic target areas can be rapidly delineated, thereby effectively narrowing the prospecting scope. In the present study, multispectral and hyperspectral satellite remote sensing data were used to extract information including linear structures, alteration anomalies, and mineral distributions in the Hod Maden and Cevizlidere areas of the Anatolian Mountains in Turkey. By analyzing the spatial distribution characteristics of alteration information and linear structures, corresponding metallogenic potential areas were predicted.

An integrated analysis of lineaments and alteration information for the Cevizlidere gold deposit, combined with the stratigraphic and lithological characteristics of the study area, allowed three prospective areas to be delineated (Figure 9). Prospective Area I is situated in the central–western part of the study area. The Cevizlidere gold deposit identified in this area is the largest porphyry Cu–Au–Mo system in Turkey. This deposit is spatially associated with a composite stock that intruded into Paleozoic limestone and Paleocene andesite on the southeastern side of the Munzur Mountains, near the southwestern margin

of the Ovacık extensional basin [18]. Within the mining district, ferruginous, clay mineral, and mica alteration anomalies are markedly concentrated, and these alteration signatures are closely associated with porphyry mineralization. Prospective Area II is situated in the central part of the study area, where the lithology is dominated by Permian metamorphic rocks and Tertiary volcanic and intrusive rocks. Two E–W-trending fault zones were interpreted in the northern and southern parts of this area. Prominent kaolinite and albite alteration anomalies occur along these fault zones, constituting typical alteration zoning characteristics of low-sulfidation epithermal deposits. Prospective Area III is situated in the northeastern part of the study area, where the lithology mainly comprises Tertiary volcanic and intrusive rocks. In this area, ferruginous alteration, pyritization, and hydroxyl alteration are concentrated, with some alteration anomalies distributed in belts along NEE-trending lineaments. Kaolinization is also observed, indicating that this area likewise has favorable metallogenic conditions.

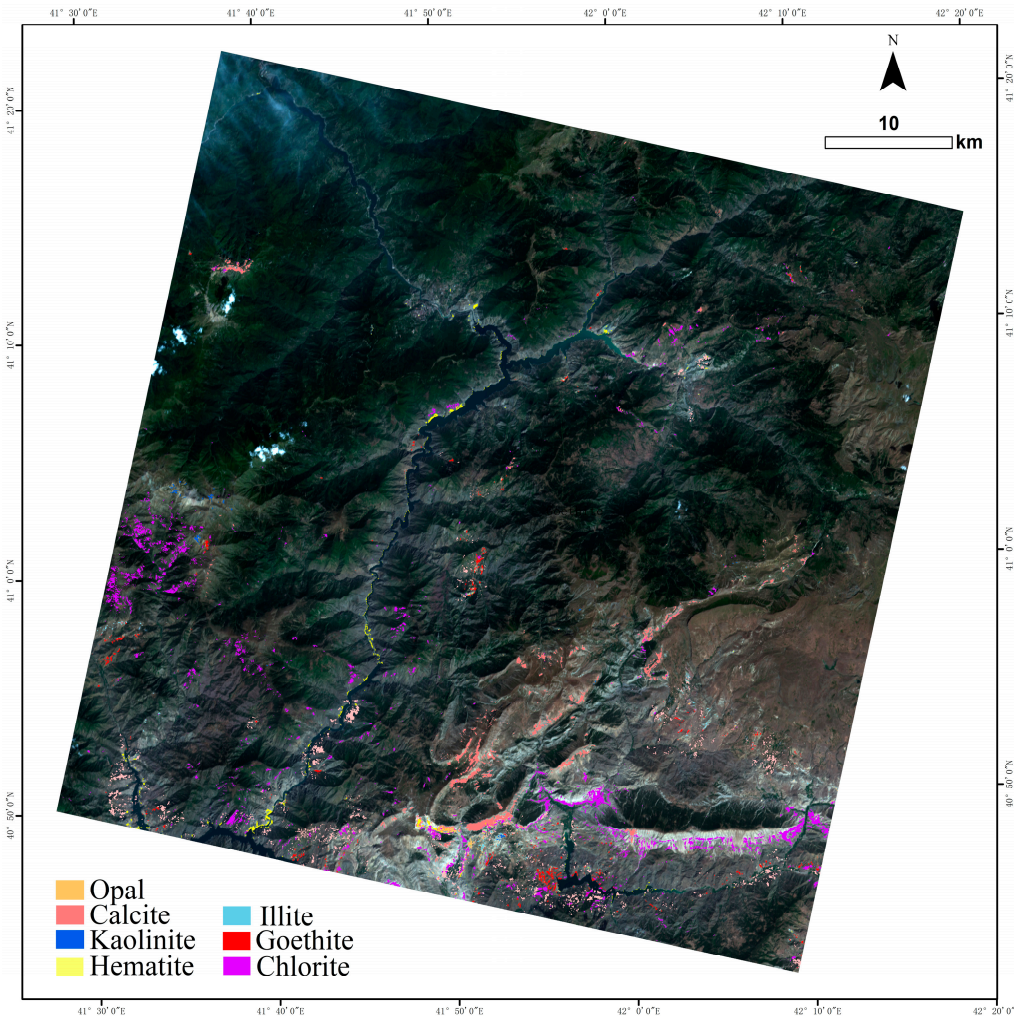


Figure 7. Alteration minerals distribution in Hod Maden derived from ZY1-02D (Basemap for display only; not original data).

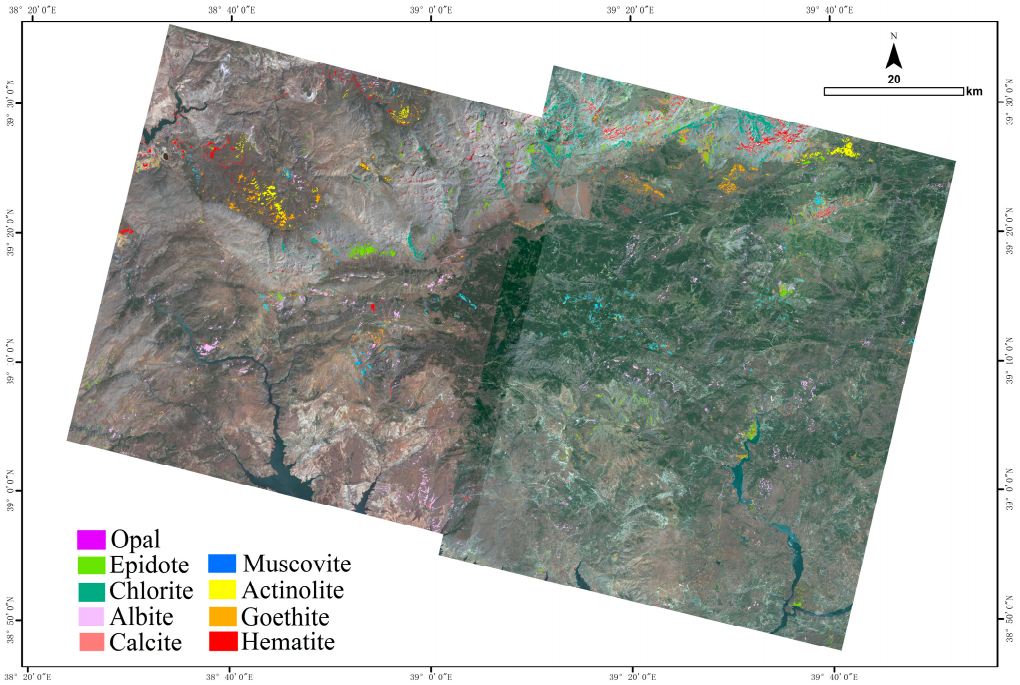


Figure 8. Alteration minerals distribution in Cevizlidere derived from ZY1-02D (**left**) and GF-5B (**right**).

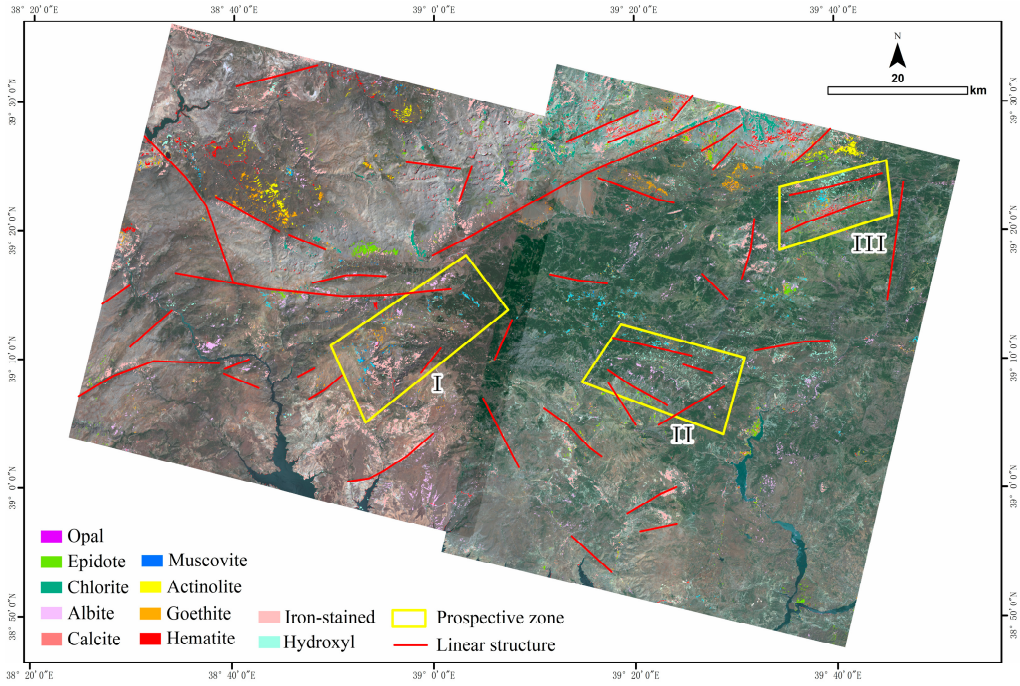


Figure 9. Prediction map of metallogenic prospective areas based on multi-source remote sensing in Cevizlidere.

Integration of lineament and alteration datasets for the Hod Maden area, together with stratigraphic and lithological constraints, facilitated the delineation of three prospective areas (Figure 10). Prospective Area I occupies the southern sector of the study area, where Early to Middle Cretaceous volcano–sedimentary successions are dominated by dacite. In this area, hydroxyl anomalies, pyritization, and chlorite–calcite alteration define belt-like distributions with strong spatial coherence, collectively denoting favorable metallogenic conditions. Prospective Area II lies in the central sector of the study area. Mineralization is

hosted within basaltic to locally dacitic volcano–sedimentary sequences, predominantly massive feldspathic breccia, locally amygdaloidal andesite, and coarse-grained andesitic breccia. A nearly N–S-striking fault zone transects this area, along which goethite and relatively intense hydroxyl anomalies are linearly arranged, whereas sparsely distributed and weaker ferruginous alteration anomalies occur in the surrounding areas. These features collectively indicate favorable conditions for shallow-seated magmatic–hydrothermal mineralization. Prospective Area III is located in the northern sector of the study area, where Late Cretaceous island-arc volcano–sedimentary successions predominate. A nearly NE-trending, deep-seated major fault zone is developed, flanked by abundant hydroxyl anomalies, with subordinate and locally developed pyritization and chloritization anomalies. These characteristics suggest considerable exploration potential for epithermal deposits in this area.

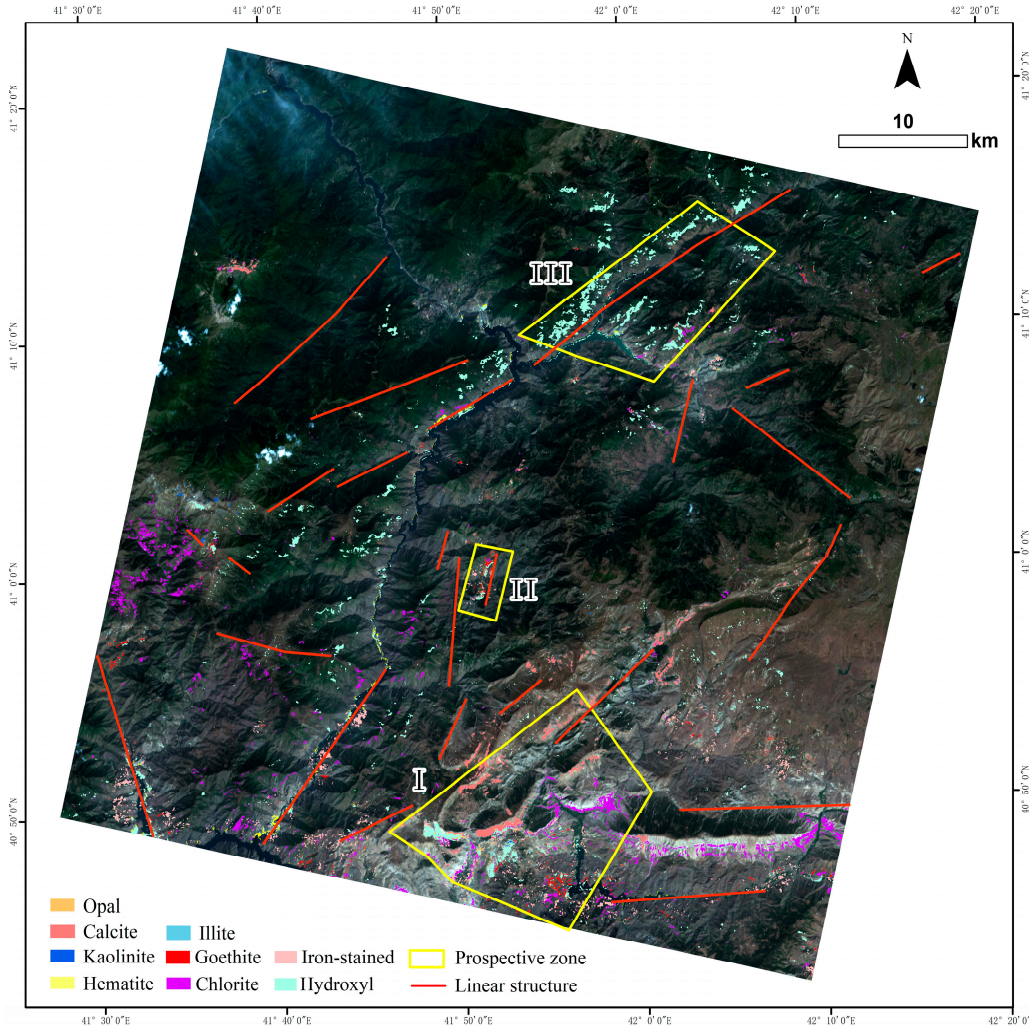


Figure 10. Prediction map of metallogenic prospective areas based on multi-source remote sensing in Hod Maden (Basemap for display only; not original data).

5. Discussion

5.1. Effectiveness of Remote Sensing for Brownfield Mineral Exploration

Evaluating the reliability of multi-source geological elements extracted solely by remote sensing in shallow overburden areas is valuable where regional geological, geophysical and geochemical data are lacking. Field reconnaissance confirms iron oxide, argillization and propylitization in the study area. Multispectral imagery, with limited bands, allows

only identification of iron-staining and hydroxyl alteration intensity anomalies through Principal Component Analysis (PCA), whereas hyperspectral imagery enables further discrimination among alteration minerals of the same type. Figures 5–8 show that multispectral alteration anomalies are spatially consistent with hyperspectral-derived minerals: high-value iron-staining zones in Figure 6 largely coincide with hematite in Figure 8, and hydroxyl-bearing minerals such as opal and chlorite correspond well with hydroxyl anomaly zones. This demonstrates the effectiveness of integrating multispectral and hyperspectral data. Nevertheless, limitations remain in vegetation-covered areas [34]. Affected by clouds and vegetation, hydroxyl anomalies in Figures 5 and 7 do not fully align with hydroxyl-bearing minerals, owing to varying cloud/vegetation coverage and mixed-pixel uncertainty; masking reduced valid pixels and may introduce statistical errors.

Linear structures are largely consistent with alteration anomalies and minerals (Figures 9 and 10). Integrating structures, alteration anomalies and mineral distribution, several prospective areas were delineated, and field reconnaissance identified gossans and leached caps (Figure 11) corresponding well with the remote sensing results. Although limitations persist in shallow-cover regions, multi-source remote sensing can still provide valuable clues for exploration.

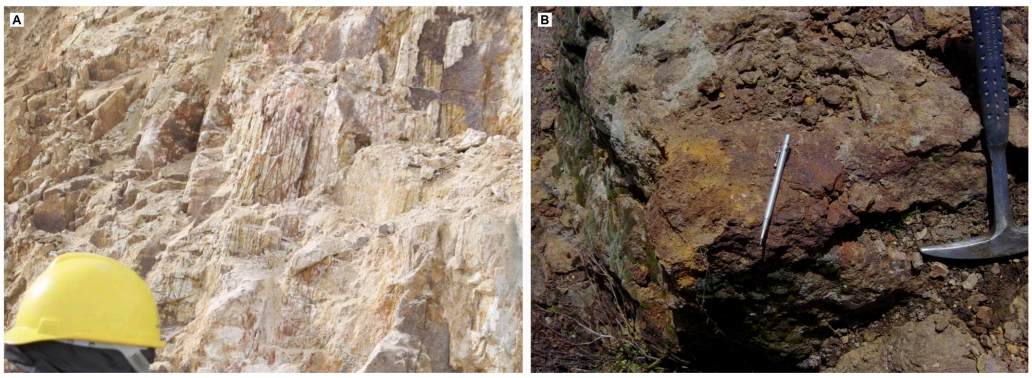


Figure 11. Alteration phenomena observed in the field ((**A**): Leached cap; (**B**): Gossan).

5.2. Limitations and Future Prospects of Remote Sensing in Exploration

Currently, the geological applications of satellite remote sensing technology are primarily focused on the interpretation of geological structures and the extraction of alteration information based on various medium- to high-spatial-resolution images, as well as the fine identification of alteration minerals using hyperspectral-resolution imagery. While such information significantly enhances the efficiency of geological exploration, the results are subject to considerable uncertainty in complex terrains due to the challenge of integrating spatial and spectral resolution. Mixed-pixel issues under intricate geological backgrounds, along with surface vegetation and cloud cover, often interfere with the acquisition of surface geological information [35]. For instance, the hyperspectral imagery obtained in the present study contains extensive vegetation coverage (Figures 7 and 8), preventing effective detection of geological information in many areas. Additionally, although airborne hyperspectral remote sensing can unify high spatial and spectral resolutions, effectively mitigating the mixed-pixel effect, its high data acquisition cost limits its widespread application [36]. To address this challenge, China is currently developing a satellite constellation plan that combines high spatial and hyperspectral resolutions. The resulting 4-m spatial resolution hyperspectral imagery will resolve existing difficulties at a low cost, greatly advancing large-scale hyperspectral remote sensing applications in geological exploration.

Airborne geophysical surveys play a crucial role in vegetation-covered areas. Airborne magnetic surveys detect magnetic ore bodies (e.g., magnetite) [37]; electromagnetic meth-

ods measure secondary fields induced by subsurface conductors [38,39]; gravity surveys identify density-contrast bodies [40]; and radiometric surveys measure gamma rays from K, U and Th decay [41]. With detection depths of tens to hundreds of meters or more, these methods penetrate vegetation and surface cover to directly reveal bedrock or deep geological bodies, their greatest advantage over optical remote sensing. However, they are costly, so integrating optical remote sensing with airborne geophysics in key metallogenic zones enables efficient acquisition and analysis of mineralization-favorable information.

Furthermore, integrating remote sensing with artificial intelligence is the primary future direction in remote sensing geology. Traditional methods rely on object–electromagnetic wave interactions using key spectral bands such as indices and PCA [3], but overlook other informative dimensions. Multimodal data challenge this cognition: Google's Alpha Earth Foundation model uses deep learning to create a unified semantic representation of optical, radar, lidar, meteorological, topographic and textual data, producing a 64-dimensional, 10-m global dataset [42]. Such imagery provides a comprehensive surface "fingerprint", and similar objects retain comparable semantic features across regions [43]. Future work could combine multimodal imagery with geologically constrained AI to train cross-region transferable models for mineral potential prediction and geological element extraction [44], improving efficiency and reducing costs.

6. Conclusions

In the present study, the Hod Maden and Cevizlidere hydrothermal metallogenic districts in Turkey were selected as case study areas to assess a fully remote sensing-driven approach for mineral exploration. The main conclusions are as follows: (1) Linear structures potentially related to mineralization were effectively identified using Sentinel-2 and high-resolution Google imagery. (2) Iron oxide and hydroxyl anomalies extracted from ASTER and Landsat data show strong spatial consistency with alteration minerals identified from hyperspectral imagery, confirming the effectiveness of multisource remote sensing for alteration analysis. (3) Integrated analysis of alteration anomalies, alteration minerals and geological structures reveals a clear correlation between the spatial distribution of multisource remote sensing-derived alteration anomalies and the orientation of linear structures. (4) Based on structural features, alteration anomalies and alteration minerals, combined with regional geological knowledge, six prospective metallogenic zones were delineated and preliminarily verified through earlier field reconnaissance. (5) Despite high vegetation cover, comprehensive analysis of geological elements driven by multisource remote sensing remains capable of supporting mineral exploration, providing a reference for remote sensing geological applications in mid- to high-altitude shallow-covered regions.

Author Contributions: Conceptualization, C.X. and X.Q.; methodology, C.X. and X.Q.; software, C.X.; validation, J.Y., D.W. and S.Z.; formal analysis, Y.P. and X.Y.; investigation, Y.Z. and C.Z.; resources, J.C.; data curation, C.X.; writing—original draft preparation, C.X.; writing—review and editing, X.Q., D.W.; visualization, H.Z. and W.X.; funding acquisition, X.Q. All authors have read and agreed to the published version of the manuscript.

Funding: This research was funded by the Deep Earth Probe and Mineral Resources Exploration—National Science and Technology Major Project of China, grant number 2024ZD1002100. This work was also supported by the China Geological Survey Project, grant number DD202606302002.

Data Availability Statement: In this research, Sentinel-2A, Landsat-9, and ASTER multispectral data were processed and downloaded from the Google Earth Engine (GEE) (https://developers.google.com/earth-engine/datasets) (accessed on 2 October 2025). The hyperspectral data was provided by the China Centre for Resources Satellite Data and Application.

Acknowledgments: The authors would like to thank the editors and the anonymous reviewers for their constructive comments and suggestions that help to enhance the clarity of the manuscript.

Conflicts of Interest: Xiaofei Yang is an employee of Civil Aviation Research Base (Beijing) Co., Ltd. The paper reflects the view of him as a researcher and not the company.

References

1. Pirajno, F. Hydrothermal Alteration. In *Hydrothermal Mineral Deposits: Principles and Fundamental Concepts for the Exploration Geologist*; Pirajno, F., Ed.; Springer: Berlin/Heidelberg, Germany, 1992; pp. 101–155, ISBN 978-3-642-75671-9.
2. Pirajno, F. *Hydrothermal Processes and Mineral Systems*; Springer: Dordrecht, The Netherlands, 2009; ISBN 978-1-4020-8612-0.
3. Shirmard, H.; Farahbakhsh, E.; Müller, R.D.; Chandra, R. A Review of Machine Learning in Processing Remote Sensing Data for Mineral Exploration. *Remote Sens. Environ.* **2022**, *268*, 112750. [CrossRef]
4. Li, S.; Romer, R.L.; Li, W.; Yang, F.; Yan, Q.; Cao, H.; Guan, S. Wall-Rock Control on the Mineral Assemblage of Hydrothermal Veins: Examples from the Mahuaping Be-W-F Deposit, Yunnan, SW China. *Ore Geol. Rev.* **2025**, *184*, 106728. [CrossRef]
5. Mo, L.; Leng, C.; Chen, X.; Zhang, X.; Li, K.; Duan, W.; Wang, Q.; Huang, S. Wall-Rock Alteration and Element Fluxes in the Disuga Porphyry Cu Deposit, Northwest Yunnan Province, China, and Implications for Mineral Exploration. *Acta Geol. Sin.-Engl. Ed.* **2025**, *99*, 1386–1403. [CrossRef]
6. Amin, B.P.; Hojjatollah, R.; Milad, S.; Mohamed, A.E.-W.; Mohammad, S.H. Remote Sensing for Mineral Exploration. In *Geospatial Analysis Applied to Mineral Exploration*; Elsevier: Amsterdam, The Netherlands, 2023; pp. 17–149.
7. Habashi, J.; Mohammady Oskouei, M.; Jamshid Moghadam, H.; Beiranvand Pour, A. Optimizing Alteration Mineral Detection: A Fusion of Multispectral and Hyperspectral Remote Sensing Techniques in the Sar-e-Chah-e Shur, Iran. *Remote Sens. Appl. Soc. Environ.* **2024**, *35*, 101249. [CrossRef]
8. Green, R.O.; Eastwood, M.L.; Sarture, C.M.; Chrien, T.G.; Aronsson, M.; Chippendale, B.J.; Faust, J.A.; Pavri, B.E.; Chovit, C.J.; Solis, M.; et al. Imaging Spectroscopy and the Airborne Visible/Infrared Imaging Spectrometer (AVIRIS). *Remote Sens. Environ.* **1998**, *65*, 227–248. [CrossRef]
9. Portela, B.; van der Werff, H.; Hecker, C.; van der Meijde, M. Landsat Next Current Design for Geological Remote Sensing: VNIR-SWIR-TIR Data Continuity and New Opportunities. *Sci. Remote Sens.* **2025**, *12*, 100258. [CrossRef]
10. Mwaniki, M.W.; Moeller, M.S.; Schellmann, G. A Comparison of Landsat 8 (OLI) and Landsat 7 (ETM+) in Mapping Geology and Visualising Lineaments: A Case Study of Central Region Kenya. *Int. Arch. Photogramm. Remote Sens. Spat. Inf. Sci.* **2015**, *XL-7-W3*, 897–903. [CrossRef]
11. Abrams, M.; Yamaguchi, Y.; Abrams, M.; Yamaguchi, Y. Twenty Years of ASTER Contributions to Lithologic Mapping and Mineral Exploration. *Remote Sens.* **2019**, *11*, 1394. [CrossRef]
12. Adiri, Z.; Lhissou, R.; El Harti, A.; Jellouli, A.; Chakouri, M. Recent Advances in the Use of Public Domain Satellite Imagery for Mineral Exploration: A Review of Landsat-8 and Sentinel-2 Applications. *Ore Geol. Rev.* **2020**, *117*, 103332. [CrossRef]
13. Sun, Y.; Tian, S.; Di, B. Extracting Mineral Alteration Information Using WorldView-3 Data. *Geosci. Front.* **2017**, *8*, 1051–1062. [CrossRef]
14. Qiao, K.; Luo, T.; Ding, S.; Quan, L.; Kong, J.; Liu, Y.; Ren, Z.; Gong, S.; Huang, Y.; Qiao, K.; et al. Extraction of Remote Sensing Alteration Information Based on Integrated Spectral Mixture Analysis and Fractal Analysis. *Minerals* **2025**, *15*, 1047. [CrossRef]
15. Hussain, M.; Li, H.; Beshr, A.M.; Memon, F.A. Remote Sensing-Based Structural and Lithological Mapping for Prospecting Polymetallic Mineralization at Xiaoshan Region, China. *Earth Sci. Inf.* **2025**, *18*, 82. [CrossRef]
16. Wang, S.; Huang, X.; Han, W.; Zhang, X.; Li, J. Geological Remote Sensing Interpretation via a Local-to-Global Sensitive Feature Fusion Network. *Int. J. Appl. Earth Obs. Geoinf.* **2024**, *135*, 104258. [CrossRef]
17. Chen, Q.; Cai, D.; Xia, J.; Zeng, M.; Yang, H.; Zhang, R.; He, Y.; Zhang, X.; Chen, Y.; Xu, X.; et al. Remote Sensing Identification of Hydrothermal Alteration Minerals in the Duobuza Porphyry Copper Mining Area in Tibet Using WorldView-3 and GF-5 Data: The Impact of Spatial and Spectral Resolution. *Ore Geol. Rev.* **2025**, *180*, 106573. [CrossRef]
18. İmer, A.; Richards, J.P.; Creaser, R.A.; Spell, T.L. The Late Oligocene Cevizlidere Cu-Au-Mo Deposit, Tunceli Province, Eastern Turkey. *Min. Depos.* **2015**, *50*, 245–263. [CrossRef]
19. Bilir, M.E.; Kuşçu, İ.; Topal, E.; Moritz, R. GEOLOGY AND STRATIGRAPHY OF HOD (ARTVİN) REGION, EASTERN PONTIDES, NE TURKEY. *Mugla J. Sci. Technol.* **2023**, *9*, 25–35. [CrossRef]
20. Callan, N.J. *Report on Geological Mapping and Prospect Evaluation, Hod Maden Property (Lic. #'s201201058, 201201059, 20050853, 201200321), Artvin Distict, NE Turkey*; Internal Aegean Metals Group Technical Report; Internal Aegean Metals Group: Vancouver, BC, Canada, 2013.
21. İmer, A.; Richards, J.P.; Creaser, R.A. Age and Tectonomagmatic Setting of the Eocene Çöpler–Kabataş Magmatic Complex and Porphyry-Epithermal Au Deposit, East Central Anatolia, Turkey. *Min. Depos.* **2013**, *48*, 557–583. [CrossRef]

22. Karaoğlan, F.; Parlak, O.; Robertson, A.; Thöni, M.; Klötzli, U.; Koller, F.; Okay, A.İ. Evidence of Eocene High-Temperature/High-Pressure Metamorphism of Ophiolitic Rocks and Granitoid Intrusion Related to Neotethyan Subduction Processes (Doğanşehir Area, SE Anatolia). *SP* **2013**, *372*, 249–272. [CrossRef]
23. Richards, J.P.; Spell, T.; Rameh, E.; Razique, A.; Fletcher, T. High Sr/Y Magmas Reflect Arc Maturity, High Magmatic Water Content, and Porphyry Cu ± Mo ± Au Potential: Examples from the Tethyan Arcs of Central and Eastern Iran and Western Pakistan. *Econ. Geol.* **2012**, *107*, 295–332. [CrossRef]
24. Chen, L.; Wang, Y.; Zhang, C. Spatial–Spectral Attention Pyramid Network for Hyperspectral Stripe Restoration. *IEEE Trans. Geosci. Remote Sens.* **2024**, *62*, 1–17. [CrossRef]
25. Gadallah, F.L.; Csillag, F.; Smith, E.J.M. Destriping Multisensor Imagery with Moment Matching. *Int. J. Remote Sens.* **2000**, *21*, 2505–2511. [CrossRef]
26. Wold, S.; Esbensen, K.; Geladi, P. Principal Component Analysis. *Chemom. Intell. Lab. Syst.* **1987**, *2*, 37–52. [CrossRef]
27. Jolliffe, I.T. *Principal Component Analysis*; Springer Series in Statistics; Springer: New York, NY, USA, 2002; ISBN 978-0-387-95442-4.
28. Crósta, A.P.; De Souza Filho, C.R.; Azevedo, F.; Brodie, C. Targeting Key Alteration Minerals in Epithermal Deposits in Patagonia, Argentina, Using ASTER Imagery and Principal Component Analysis. *Int. J. Remote Sens.* **2003**, *24*, 4233–4240. [CrossRef]
29. Hunt, G.R. Spectral Signatures of Particulate Minerals in the Visible and near Infrared. *Geophysics* **1977**, *42*, 501–513. [CrossRef]
30. Wang, D.; Chen, J.; Dai, X. Extracting Geological and Alteration Information and Predicting Antimony Ore Based on Multisource Remote Sensing Data in Huangyangling, Xinjiang. *Front. Earth Sci.* **2024**, *12*, 1366727. [CrossRef]
31. Clark, R.N.; King, T.V.V.; Klejwa, M.; Swayze, G.A.; Vergo, N. High Spectral Resolution Reflectance Spectroscopy of Minerals. *J. Geophys. Res. Solid Earth* **1990**, *95*, 12653–12680. [CrossRef]
32. Kruse, F.A.; Lefkoff, A.B.; Boardman, J.W.; Heidebrecht, K.B.; Shapiro, A.T.; Barloon, P.J.; Goetz, A.F.H. The Spectral Image Processing System (SIPS)—Interactive Visualization and Analysis of Imaging Spectrometer Data. *Remote Sens. Environ.* **1993**, *44*, 145–163. [CrossRef]
33. Chen, Q.; Cai, D.; Zhao, Z.; Yang, X.; Wang, Y.; Jiang, X.; Xu, L.; Duan, H.; He, Y.; Zhang, X.; et al. Alteration Information Extraction and Mineral Prospectivity Mapping in the Laozhaiwan Area Using Multisource Remote Sensing Data. *Remote Sens.* **2025**, *17*, 2178. [CrossRef]
34. Mahanta, P.; Maiti, S. Remote Detection of Hydrothermal Alteration Zones Using WorldView-3 VNIR-SWIR Reflectance Data: A Study from Lawa Gold Mines, India. *J. Indian Soc. Remote Sens.* **2022**, *50*, 1979–1993. [CrossRef]
35. Zhang, H.; Duan, L.; Zhang, Y.; Li, H.; Li, D.; Li, Y.; Zhang, H.; Duan, L.; Zhang, Y.; Li, H.; et al. Applicability Analysis with the Improved Spectral Unmixing Models Based on the Measured Hyperspectral Data of Mixed Minerals. *Minerals* **2025**, *15*, 715. [CrossRef]
36. Xu, Q.; Liu, S.; Ye, F.; Zhang, Z.; Zhang, C. Application of CASI/SASI and Fieldspec4 Hyperspectral Data in Exploration of the Baiyanghe Uranium Deposit, Hebukesaier, Xinjiang, NW China. *Int. J. Remote Sens.* **2018**, *39*, 453–469. [CrossRef]
37. Prikhodko, A.; Bagrianski, A.; Wilson, R.; Belyakov, S.; Esimkhanova, N. Detecting and Recovering Critical Mineral Resource Systems Using Broadband Total-Field Airborne Natural Source Audio Frequency Magnetotellurics Measurements. *Geophysics* **2023**, *89*, WB13–WB23. [CrossRef]
38. Fu, C.; Zhang, S.; Song, Y.; Wei, H.; Xue, C.; Chen, J. Data-Driven Copper Prospectivity Mapping across Iran Using an Interpretable Maximum Entropy Modeling. *Ore Geol. Rev.* **2025**, *187*, 107024. [CrossRef]
39. Liang, S.; Sun, S.; Lu, H.; Liang, S.; Sun, S.; Lu, H. Application of Airborne Electromagnetics and Magnetics for Mineral Exploration in the Baishiquan–Hongliujing Area, Northwest China. *Remote Sens.* **2021**, *13*, 903. [CrossRef]
40. Kwan, K.; Reford, S. Innovative Airborne Geophysical Strategies to Assist the Exploration of Critical Metal Systems. *Geosystems Geoenvironment* **2025**, *4*, 100344. [CrossRef]
41. Liao, G.; Li, Y.; Xi, Y.; Lu, N.; Wu, S.; Liao, G.; Li, Y.; Xi, Y.; Lu, N.; Wu, S. Application of High-Resolution Aeromagnetic and Gamma-Ray Spectrometry Surveys for Litho-Structural Mapping in Southwest China. *Minerals* **2023**, *13*, 1424. [CrossRef]
42. Brown, C.F.; Kazmierski, M.R.; Pasquarella, V.J.; Rucklidge, W.J.; Samsikova, M.; Zhang, C.; Shelhamer, E.; Lahera, E.; Wiles, O.; Ilyushchenko, S.; et al. AlphaEarth Foundations: An Embedding Field Model for Accurate and Efficient Global Mapping from Sparse Label Data. *arXiv* **2025**, arXiv:2507.22291.
43. Qin, Q. AlphaEarth Foundations: The Potential and Challenges of Remote Sensing Foundation Models. *J. Geo-Inf. Sci.* **2025**, *27*, 2283–2290. [CrossRef]
44. Wang, L.; Li, T.; Wu, S.; Yang, J.; Hu, Y.; Hu, L.; Chen, Y.; Ge, Y.; Chen, Y.; Rao, C.; et al. Geologically Constrained Data-Driven Modeling for Mineral Prospectivity Mapping. *Geology* **2025**, *54*, 225–230. [CrossRef]

Disclaimer/Publisher's Note: The statements, opinions and data contained in all publications are solely those of the individual author(s) and contributor(s) and not of MDPI and/or the editor(s). MDPI and/or the editor(s) disclaim responsibility for any injury to people or property resulting from any ideas, methods, instructions or products referred to in the content.